Dense water formation on the northwestern shelf of the Okhotsk Sea: 2. Quantifying the transports

Andrey Y. Shcherbina, Lynne D. Talley, and Daniel L. Rudnick
Scripps Institution of Oceanography, University of California, San Diego, La Jolla, California, USA

Received 10 November 2003; revised 26 April 2004; accepted 17 May 2004; published 8 July 2004.

[1] A combination of direct bottom mooring measurements, hydrographic and satellite observations, and meteorological reanalysis was used to estimate the rate of formation of Dense Shelf Water (DSW) due to brine rejection on the Okhotsk Sea northwestern shelf and the rate of export of DSW from this region. On the basis of remote sensing data, an estimated 8.6×10^{12} m^3 of DSW was formed during the winter of 1999–2000, resulting in a mean annual production rate of 0.3 Sv. According to direct observations, the export rate of DSW during this period varied from negligibly small in autumn to 0.75 ± 0.27 Sv in winter (January–February), to 0.34 ± 0.12 Sv in spring (March–April). From these observations the mean annual export rate can be estimated to be 0.27 Sv. The same relationships used to obtain the integral estimates were also applied differentially using an advective approach incorporating realistic flow and heat flux fields, which allowed direct comparison with the moored observations. The comparison highlights the importance of along-shelf advection and cross-shelf eddy transport to the accurate parameterization of DSW formation. *INDEX TERMS:* 4207 Oceanography: General: Arctic and Antarctic oceanography; 4540 Oceanography: Physical: Ice mechanics and air/sea/ice exchange processes; 4283 Oceanography: General: Water masses; 4219 Oceanography: General: Continental shelf processes; *KEYWORDS:* Okhotsk Sea, dense water formation, transport

Citation: Shcherbina, A. Y., L. D. Talley, and D. L. Rudnick (2004), Dense water formation on the northwestern shelf of the Okhotsk Sea: 2. Quantifying the transports, *J. Geophys. Res.*, *109*, C09S09, doi:10.1029/2003JC002197.

1. Introduction

[2] The Okhotsk Sea is known to be the origin of the densest water mass formed in the North Pacific, its intermediate water (NPIW) [*Talley*, 1991, 1993; *Yasuda*, 1997]. The initial overturn is driven by brine rejection during ice formation in the northern coastal polynyas, leading to production of cold ($\theta < -1$°C), oxygen-rich dense shelf water (DSW) with densities of up to 26.7–27.2σ_θ [*Kitani*, 1973; *Gladyshev et al.*, 2000].

[3] A chain of persistent polynyas (Figure 1) occurs along the northern and northwestern shelves of the Okhotsk Sea each winter due to the offshore winds. Intense heat loss inside the polynyas leads to intense ice formation and brine rejection into underlying waters. Newly formed DSW is advected by the large-scale wind-driven cyclonic circulation in the basin while each polynya in turn contributes to the density increase. The northwestern polynya (NWP) finishes this process, after which the DSW is transported southward by the East Sakhalin Current.

[4] Annual formation of DSW gives rise to a layer of Okhotsk Sea mode water (OSMW) in the 26.7–27.0 σ_θ potential density range, characterized by low potential vorticity and high oxygen content [*Yasuda*, 1997]. *Gladyshev et al.* [2000] estimated the DSW contribution to OSMW to be 25 to 45% in the 26.65–26.85 σ_θ range. OSMW is subsequently modified in the Kuril Basin, where the Soya Warm Current water affects the upper OSMW, and vertical mixing extends its signature downward to 27.1–27.6 σ_θ [*Kitani*, 1973; *Talley*, 1991; *Gladyshev et al.*, 2003]. OSMW is eventually exported into the open ocean through Bussol' Strait leading to the ventilation of NPIW in both the subpolar and subtropical gyres.

[5] Estimation of the dense shelf water formation rates is consequently important for parameterization of the whole downward branch of the North Pacific thermohaline circulation. *Yasuda* [1997] estimated a rate of outflow of OSMW through the Bussol' Strait of 1.1 ± 0.8 Sv (1 Sv = 10^6 m^3 s^{-1}), which would require a net production of 0.4 ± 0.3 Sv of DSW per year. Using a simple box model involving CFC data, *Wong et al.* [1998] estimated a much larger DSW formation rate of 0.9–9.4 Sv. *Martin et al.* [1998] and *Gladyshev et al.* [2000], using remotely sensed ice production rates and non-winter hydrographic surveys, respectively, estimated annual DSW formation rates between 0.2 and 0.5 Sv, depending on the winter conditions for a given year. Seasonal change in the DSW outflow from 1.4 ± 1.2 Sv during February–May to 0.2 ± 0.1 Sv in summer, with an annual average of 0.6 ± 0.6 Sv, has also been suggested by historical hydrographic data analysis for the Kuril Basin [*Gladyshev et al.*, 2003]. Another analysis of historical data [*Itoh et al.*, 2003] further supports these results, yielding a mean annual DSW formation rate of 0.67 Sv.

0148-0227/04/2003JC002197$09.00

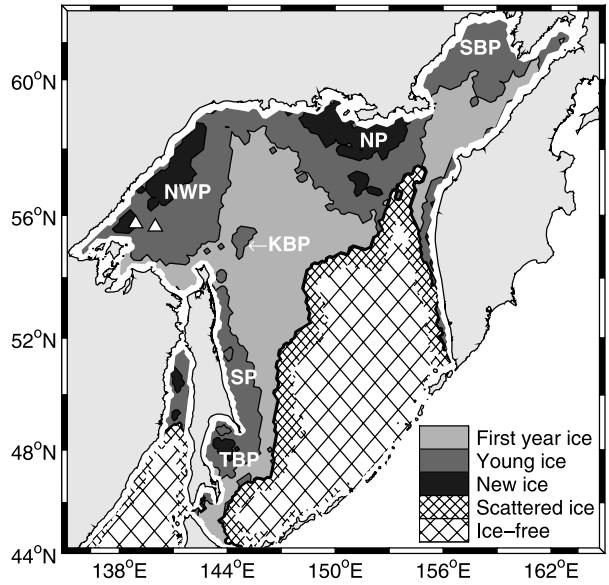

Figure 1. Ice distribution in the Okhotsk Sea on 1 February 2000, showing the persistent polynyas: Shelikhov Bay (SBP), northern (NP), northwestern (NWP), Kashevarov Bank (KBP), Sakhalin (SP), and Terpeniya Bay (TBP). Ice classification is based on National Snow and Ice Data Center SSM/I brightness temperatures. White triangles show the bottom mooring positions.

[6] The present study estimates the rates of DSW formation and export during the winter of 1999–2000 using both satellite and in situ wintertime observations (section 2). The relationship of surface heat loss to densification of shelf waters is also investigated using the advective approach with the flow and heat flux fields based on observations (section 3). The data sets are described by *Shcherbina et al.* [2003, 2004].

2. Estimating DSW Formation and Export Rates

[7] Using a combination of remote and in situ observations, we attempt to construct a comprehensive image of the evolution of DSW on the northwestern shelf, relating the independent estimates of formation and export rates of this water mass. First, we use the surface heat loss based on the ice distribution and meteorology fields to estimate the salt enrichment due to ice formation, allowing the approximation of DSW formation rate (section 2.1). Second, the export rates are estimated using moored velocity data and assumptions of the DSW cross-section area based on hydrographic data (section 2.2). Both estimates are combined in section 2.3 in a simple production-export model.

2.1. Formation Rates of DSW Based on Satellite and Reanalysis Data

[8] Indirect methods of estimation of brine rejection and mixing rates based on remote sensing and/or water mass analysis are the only means of studying dense water formation in most polynyas worldwide. Our moorings provide a rare opportunity to compare and combine the direct and indirect methods.

[9] The first estimates of dense water formation on the northwestern shelf of the Okhotsk Sea based on Special Sensor Microwave/Imager (SSM/I) ice concentration and National Centers for Environmental Prediction (NCEP) reanalysis meteorological data were made by *Alfultis and Martin* [1987] and *Martin et al.* [1998]. *Ohshima et al.* [2003] suggested an improved heat flux calculation algorithm incorporating an accurate treatment of heat fluxes through different ice types, and calculated the surface heat balance for the entire Okhotsk Sea.

[10] The heat flux estimation algorithm used in the present study (Appendix A) generally follows that of *Ohshima et al.* [2003]. The main differences in our algorithm are the parameterization of ice thickness as a continuous function of ice-type parameter instead of ascribing the thickness to three discrete ice types [*Ohshima et al.*, 2003], and choice of slightly different radiative heat flux parameterizations that were shown to be appropriate for arctic conditions [*Key et al.*, 1996]. The main benefit of using bulk parameterization of heat fluxes based on reanalyzed lower atmosphere meteorology and SSM/I ice data over the output of large-scale meteorological reanalysis models is the improvement of the resolution of ice cover and distinguishing between the various ice types. Sea ice distribution was determined using the 25-km gridded SSM/I brightness temperature data [*Maslanik and Stroeve*, 2003].

[11] For each pixel the total ice concentration and ice type were derived using the thin ice algorithm [*Cavalieri*, 1994] from the 19/37 GHz gradient ratio $Gr = (T_{37V} - T_{19V})/(T_{37V} + T_{19V})$ and 19 GHz polarization ratio $Pr = (T_{19V} - T_{19H})/(T_{19V} + T_{19H})$, where T_{37V}, T_{19V}, and T_{19H} are the vertically polarized 37 GHz and vertically and horizontally polarized 19 GHz SSM/I brightness temperatures, respectively. Algorithm tie points suitable for the Okhotsk Sea conditions [*Martin et al.*, 1998] were used. Three ice types, namely new, young, and first-year ice, were distinguished using the 19 GHz polarization ratio [*Kimura and Wakatsuchi*, 1999]. These ice types (as well as the open water) were ascribed different radiative and thermodynamic properties, leading to different parameterizations of surface heat fluxes. The particular differences are mentioned in Appendix A.

[12] The estimate of heat loss F at the ice surface takes into account turbulent sensible (F_S), latent or evaporative (F_L), and net shortwave (S) and longwave (L) heat fluxes,

$$F = F_S + F_E + F_R + F_L. \quad (1)$$

The fluxes are calculated using the low-resolution (~1.125 degree) ECMWF reanalysis meteorological data (10-m wind speed, 2-m air temperature, and surface atmospheric pressure) and high-resolution (25 km) ice type data (see Appendix A for details). The free parameter of these calculations is the ice surface temperature T_s, which is determined by balancing the surface heat loss with the conductive heat flux through the ice.

[13] The heat flux algorithm suffers greatly from large uncertainties in bulk heat parameterization, especially since very little opportunity for direct verification of flux estimates exists. Uncertainties in ice concentration, air temperature, and wind speed are the most important sources of error in winter [*Ohshima et al.*, 2003]. Additionally, the wintertime heat flux estimate is greatly dependent on the parameterization of thickness and thermal properties of sea ice [*Ohshima et al.*, 2003]. The primary source of error is the use of direct semi-empirical relationships of ice thick-

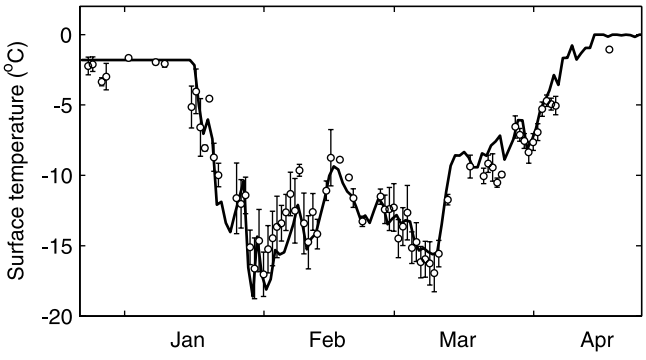

Figure 2. Ice surface temperature inferred via heat balance (line) and observed by AVHRR (dots). Average within a 50 km radius of 146°E 57°N is shown. One standard deviation error bars are shown for AVHRR data.

ness to the ice type, while the SSM/I ice classification is strongly affected by seasonal and regional variability of radiative properties of ice surface. As a simple consistency test, the ice surface temperatures that were obtained as a by-product of heat balance estimates were compared with the surface temperatures T_{SST}, obtained by NOAA/NASA Polar Pathfinder Advanced Very High Resolution Radiometer (AVHRR) (C. Fowler et al., AVHRR Polar Pathfinder twice-daily 5 km EASE-Grid composites, available from National Snow and Ice Data Center at http://nsidc.org/data/nsidc-0066.html, 2000, updated 2002). Significant cloud cover over the area in wintertime made reliable AVHRR data scarce, so an area-averaged approach had to be taken.

[14] The heat flux method tends to underestimate the ice surface temperature in the first half of the winter (compared to AVHRR data, which is assumed to be correct), and overestimates it in the second half (Figure 2). The domain-averaged difference between T_s and T_{SST} varied from about -1.5°C in early January to 0.4°C in April. Standard deviation of the difference $T_s - T_{SST}$ ranged from 1°C to 3°C, with the maximum in late January when the diversity of ice types was the greatest. Overestimation of T_s might have resulted from the buildup of snow on the ice surface as it ages. Snow cover provides additional insulation, decreasing the conductive heat flux and surface temperature measured by AVHRR. SSM/I ice classification, however, does not fully account for this cover, and consequently the conductive heat flux and the ice surface temperature may be overestimated for the case of old snow-covered ice. Older ice, however, contributes little to the total heat loss compared to the young polynya ice, which is usually free from substantial snow cover. Consequently, snow cover effects were not included in our heat flux estimate.

[15] The satellite observations provide an independent method of validation of the heat flux algorithm, and could potentially enable the further calibration of ice thickness classification. However, the scarcity of clear-sky AVHRR images during the winter did not allow such calibration for the present study.

[16] Without knowledge of the water temperature distribution, it is not possible to determine if the heat loss leads to ice formation. In the present study we assume that the water in the immediate vicinity of ice is close to freezing, so the heat loss in pixels where ice is already present is translated into ice formation. On the other hand, we assume that water in ice-free pixels is too warm and that no significant ice formation occurs there, even though such an assumption underestimates the ice production at the initial stages of freezing. The ice concentration throughout the polynya region was high from mid-January to the end of April, so the exclusion of open-water ice production is not expected to affect the estimate of the rate of DSW formation happening mainly during this period.

[17] Following *Cavalieri and Martin* [1994] (hereinafter referred to as CM-94) and *Martin et al.* [1998], the ice volume production (V_i), salt flux (S_F), and dense water volume production in the polynya (V_{DSW}) are given by (per unit area)

$$V_i = \frac{F}{\rho_i L}, \tag{2}$$

$$S_F = \rho_i V_i (s_0 - s_i) 10^{-3}, \tag{3}$$

$$V_{DSW} = \frac{S_F}{(\rho_b s_b - \rho_0 s_0) 10^{-3}}, \tag{4}$$

where F is the net surface heat loss, $\rho_i = 920$ kg m^{-3} is the ice density, $L = 2.34 \times 10^5$ J kg^{-1} is the latent heat of fusion of sea ice, s_i is the ice salinity, $\rho_0 = 1026.25$ kg m^{-3} ($\rho_b = 1026.9$ kg m^{-3}) and $s_0 = 32.6$ psu ($s_b = 33.4$ psu) are water density and salinity before (after) the density enrichment by brine rejection. Note that compared to *Martin et al.* [1998], a lower L, which is more appropriate for salt-water ice production [*Haarpaintner et al.*, 2001], as well as lower s_0 and ρ_0 consistent with the observed values [*Shcherbina et al.*, 2004], are used. Following CM-94, constant ice salinity $s_i = 0.31 s_0$ is assumed.

[18] The obtained DSW production rates were integrated over the northwestern polynya region. For the purpose of this study, this region was empirically defined by the box shown in Figure 3a. Approximately the same definition was used by *Martin et al.* [1998] and *Gladyshev et al.* [2000].

[19] The estimated mean heat loss within the northwestern polynya during the winter of 1999–2000 was on the order of 100 W m^{-2}. It reached a maximum of about 190 W m^{-2} by the end of January (Figure 3b). A brief polynya closure happened on 15 February, after which the heat loss continued at a rate of about 85 W m^{-2} until 10 March. After 15 March the polynya region was covered with thick first-year ice and the heat loss dropped to about 20 W m^{-2}. The estimated heat flux corresponds to the formation of a total of 8.6×10^{12} m^3 of DSW in the NWP alone, which corresponds to the mean annual production rate of 8.6×10^{12} m^3/12 month = 0.27 Sv. Formation rates varied between 2.28 Sv in late January and 0.98 Sv in early March.

[20] It should be mentioned that the error in the net heat flux estimate associated with the uncertainties in atmospheric forcing and ice conditions is on the order of at least 20 W m^{-2} [*Ohshima et al.*, 2003]. Consequently, our estimates of DSW production have approximately 25% error margin.

2.2. Export Rates of DSW Based on In Situ Data

[21] The properties of DSW and the flow field in the southern part of NWP were observed directly by bottom

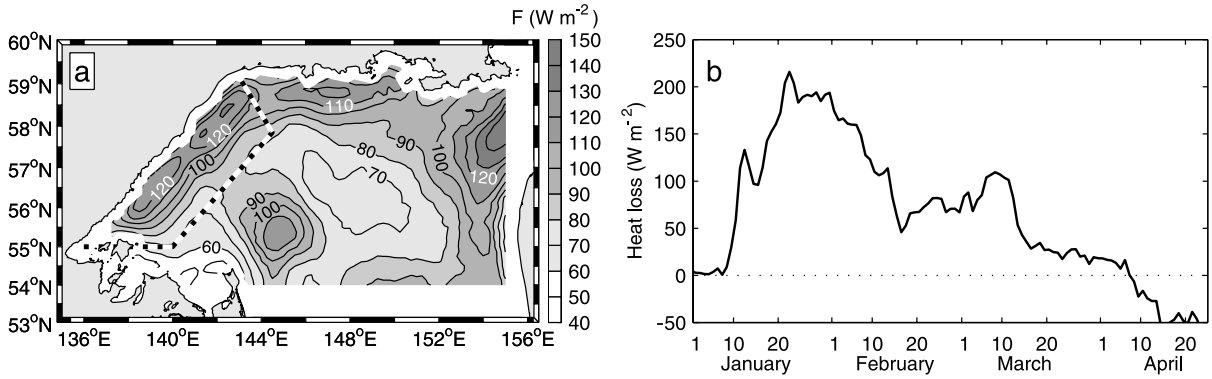

Figure 3. (a) Surface heat loss in the northern Okhotsk Sea (average over the period from 10 January to 10 April 2000). (b) Time series of mean heat loss from the northwestern polynya region (marked with dashed line in Figure 3a). Heat loss in absence of ice formation is disregarded.

moorings during the winter of 1999–2000 [*Shcherbina et al.*, 2004]. The velocities measured by Acoustic Doppler Current Profilers (ADCP) at the moorings combined with the assumptions about the DSW extent (Figure 4) can be used to estimate the rate of export of this water mass from its formation region.

[22] The outer margin of dense water was found to be located between the two moorings during the ice-cover season (January–March) based on the fact that the significant density increase associated with DSW formation was observed by only the inshore instrument [*Shcherbina et al.*, 2003, 2004]. Additionally, we assume that the new dense water extended all the way to shore and to the surface as a result of vigorous brine-driven convection in that region (Figure 4b). Consequently, the DSW cross section during this period can be estimated as $(12.5 \pm 4.5) \times 10^6$ m^2, with the uncertainty being half the cross-section area between the two instruments. The flow through the section is assumed to have been uniform, since the mean velocities observed by the two moorings were nearly identical [*Shcherbina et al.*, 2004]. With a mean advection velocity of 6 cm s^{-1} (January–February), the winter dense water transport was roughly 0.75 ± 0.27 Sv. The transport dropped to about 0.34 ± 0.12 Sv in spring (March–April) due to decreased velocity.

[23] A more reliable estimate of the dense water cross section is possible at the times of the two hydrographic sections, occupied during the mooring deployment and recovery cruises in September 1999 and June 2000. On these sections, DSW stands out as a well-mixed water mass bounded by sharp property gradients [*Shcherbina et al.*, 2004], which allows its clear demarcation. Similarly to *Gladyshev et al.* [2003], we define DSW as water denser than 26.7 σ_θ, as brine rejection is the primary source of ventilation of OSMW in that density range. Additionally, we use the −1°C isotherm to bound DSW laterally (Figures 4a and 4c). (On our sections, the 0°C isotherm used by *Gladyshev et al.* [2003] lay outside the temperature gradient surrounding the DSW.) The cross section of DSW, defined in this way, was 6.9×10^6 m^2 in September and 7.7×10^6 m^2 in June (Figures 4a and 4c). Mean velocities are taken from the first and last week of the record of the offshore mooring, since it was located in the core of the dense water during these periods. The resulting estimate is 0.33 Sv in June and close to 0.02 Sv in September.

2.3. Combined Results: Production-Export Model

[24] The changes of net volume of DSW on the northwestern shelf can be parameterized by the difference of the formation and export rates estimated in the previous sections, as illustrated in Figure 5. In this calculation, dense water is assumed to be absent from the shelf at the beginning of the ice formation period, which is consistent with the observations [*Shcherbina et al.*, 2004]. Import of dense water from northern polynyas, though hardly negligible, is not included. After the rapid increase in January–February, the DSW volume stayed almost constant from 10 March to 5 April. Maximum DSW volume reached during that period was 4.8×10^{12} m^3, which is approximately half of the total volume (8.6×10^{12} m^3) of new DSW formed in that region. Gradual flushing of dense water from the shelf continued after the formation ceased in early April.

3. Advective Approach to the Production-Export Balance

[25] The unique feature of the present experiment is the presence of wintertime observations of bottom water properties in the polynya region [*Shcherbina et al.*, 2003]. These observations [*Shcherbina et al.*, 2004] can potentially provide a necessary direct verification of the methods used to obtain the DSW formation and export rates in section 2.1. However, direct comparison of these integral estimates with the point mooring measurements is not possible. In order to reconcile the two approaches, the same production-export balance applied previously to the DSW as a whole can be extended to study the evolution of individual infinitesimal parts of it, explicitly considering the effect of advection through a spatially and temporally varying polynya region.

[26] For this purpose we consider a large number of "particles" in an idealized horizontal advection field. Each particle represents a water column with unit cross section and is characterized by its salinity. The salinity of the particles changes as they travel under the actual spatially inhomogeneous and time-varying salinity flux field S_F, which was calculated in the previous section based on

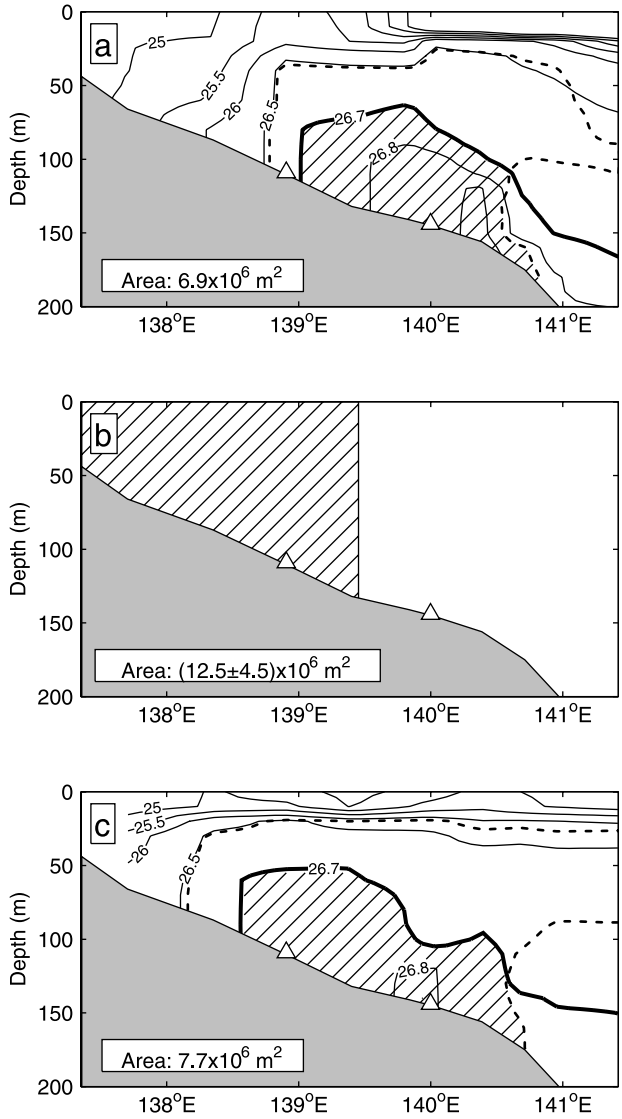

Figure 4. Estimated DSW cross section (hatching) in (a) autumn, (b) winter, and (c) spring. Solid contours in Figures 4a and 4c show potential density distribution in September 1999 and June 2000, respectively. Thicker contours correspond to σ_θ = 26.7 isopycnals. Dashed contours show −1°C isotherm. Open triangles indicate the location of bottom moorings.

remote ice sensing and meteorology. Instantaneous mixing to the bottom is assumed, so the evolution of the salinity of a particle with time t is approximated by

$$s = \int \frac{10^3 S_F(\mathbf{x}, t)}{\rho_0 h(\mathbf{x})} dt, \tag{5}$$

where $\mathbf{x} = \mathbf{x}(t)$ is the position of the particle, S_F is the salt flux and $h(\mathbf{x})$ is the local water depth.

[27] This advective estimate for salinity change is compatible with the CM-94 algorithm in terms of integral rates of salt influx and export. At the same time, the advective approach provides an improved view of the evolution of water properties throughout the brine rejection period. This approach accounts for the cumulative effect of spatially varying brine rejection and variations in water residence time inside the polynya. Most importantly, since the salinity of the particles passing through a certain point can be tracked, direct comparison of the estimated rate of salinity increase with the moored observations is possible. As a result, the rates of brine rejection estimated from heat fluxes can be independently verified, providing a test of the CM-94 algorithm.

3.1. Advection Field

[28] In the absence of comprehensive observed or modeled velocity climatology, an artificial advection field is constructed based as much as possible on the flow observed at the moorings [*Shcherbina et al.*, 2003, 2004]. Without forcing or friction, the stream function ψ of geostrophic unstratified flow satisfies

$$\nabla\psi\nabla(f/h) = 0, \tag{6}$$

where f is the Coriolis parameter and h is the ocean depth [*Pedlosky*, 1987]; that is, the flow has to follow lines of constant planetary potential vorticity f/h. The mean velocities observed at the moorings were generally directed along the contours of f/h (Figure 6), roughly supporting the above hypothesis. The solution of equation (6) is

$$\psi = \Psi(f/h), \tag{7}$$

where Ψ is an arbitrary function that must be determined using the information of the cross-shore flow variation. Similarly to the assumptions of section 2.2, the flow across the line connecting the moorings is assumed to be uniform. This assumption is justified by high correlation of the flow measured by the moorings [*Shcherbina et al.*, 2004], and it is minimally sufficient for definition of Ψ up to an arbitrary multiplier. Such choice of Ψ results in relatively uniform velocity over the northern and northwestern shelves with intensifications in the regions of the East Sakhalin and Kamchatka Currents as well as in the northeastern corner of the basin (Figure 7a).

[29] We wish to evaluate the possible role of circulation changes in DSW evolution. The constructed velocity field was therefore modulated in time so that its value at the site of the inshore mooring matches the vertically averaged velocity observed at that location [*Shcherbina et al.*, 2004], low passed using a 72-hour Blackman filter (Figure 7b). This modulation affects only the absolute values but not the direction of the flow, so the general flow pattern remains invariant (although it reverses in several instances). The particles are advected using the fourth-order Runge-Kutta scheme with a 1-day time step. We reiterate that this scheme is introduced as a simple observation-based refinement of the bulk DSW production estimate (section 2), and is not meant to be a full simulation of the Okhotsk Sea circulation.

3.2. Monte Carlo Simulation

[30] The domain was initially populated with 10,000 particles randomly distributed throughout the basin. The initial salinity of all particles was set to s_0 = 32.6 psu to match the assumed initial salinity of DSW, based on the

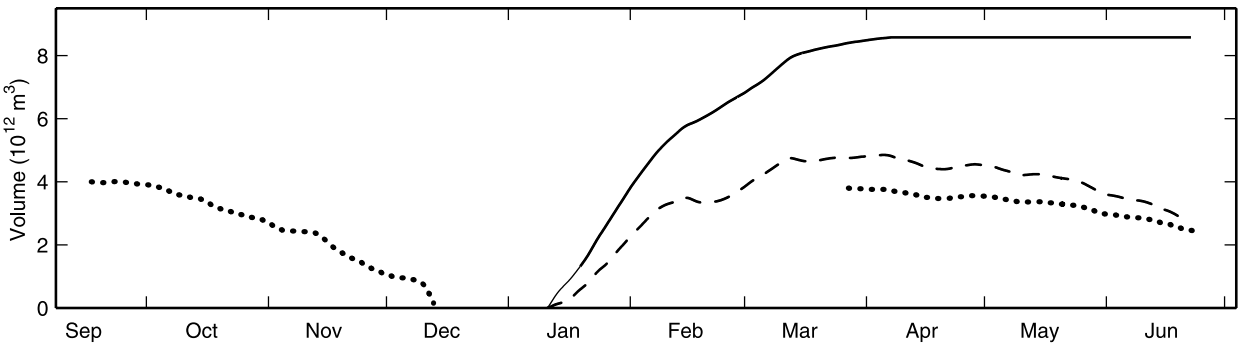

Figure 5. Volume of DSW in the NWP region estimated via brine rejection rates based on SSM/I ice concentration data and ECMWF reanalysis meteorology (solid black line). The same estimate but corrected for the wintertime export, estimated in section 2.1 using the moored velocity data (dashed black line). Integrals of fall and spring export estimates based on hydrographic data and moored velocity data (dotted lines) are shown for reference, arbitrarily offset.

moored observations [*Shcherbina et al.*, 2004]. (This initial salinity is also consistent with that used in section 2.1.) Particles that left the domain during the run were reintroduced at a random location within the ''repopulation'' region upstream of the polynya (Figure 7a), representing freshwater inflow. The salinity of reintroduced particles was set to be s_0 as well.

3.3. Comparison With Direct Observations

[31] The advective approach to the production-export balance captures the general tendencies of dense water formation due to brine rejection (Figure 8), validating the CM-94 parameterization of dense water formation based on surface heat fluxes. At the same time, several discrepancies between the observed and estimated salinity variations clearly show the limits of applicability of the simple production-export balance in both advective (differential) and integral forms.

[32] The advective estimate of salinity increase at the site of the inshore mooring was 26% slower (0.017 psu/day versus 0.023 psu/day), but continued considerably longer than was actually observed at that site. As a result, the total salinity increase was overestimated by 22% by the advective method. The slower salinity increase suggests that the estimate (equation (3)) of the salt flux associated with ice formation is biased low by a factor of 0.74, which is not unreasonable given the uncertainties in the heat flux parameterization (section 2.1). If the salt flux were adjusted so that the rates of salinity increase match the observations, the estimate of mean annual DSW formation rate made in section 2.1 would increase to 0.36 Sv. Total DSW salinity increase would be overestimated by 70% in that case, due to the longer period of salinity increase inferred from the heat fluxes.

[33] The duration of the dense water formation yielded by the advective approach depends mostly on the duration of the polynya opening rather than the heat flux parameterization. Consequently, this method can be expected to predict the dates of the beginning and end of DSW formation more accurately than the amount of the salinity increase, as the former estimates are the most direct ones. Nonetheless, the advective approach predicts the salinity increase at the inshore mooring site starting at least a week earlier and terminating almost a month later than was actually observed.

[34] One of the factors missing from both the CM-94 formation estimate (section 2) and the advective estimate is the initial background stratification of the water column. The delayed onset of density increase at the bottom can be readily explained by the time necessary to overcome such stratification. It also may explain why a much slower salinity increase was observed at the offshore (deeper) mooring. The salinity observed at the offshore mooring in January was higher than the maximum salinity predicted by the advective approach for the brine rejection season (Figure 8). If the latter were indeed the maximum brine salinity at that location, the convection plume would not reach the bottom there. Consequently, late autumn stratification likely played a crucial role controlling the extent of bottom penetration of the newly formed DSW.

[35] Additionally, estimates of DSW export based on the mooring data do not account for cross-shelf eddy transport of density anomalies. As shown by modeling studies [*Gawarkiewicz and Chapman*, 1995], geostrophic adjust-

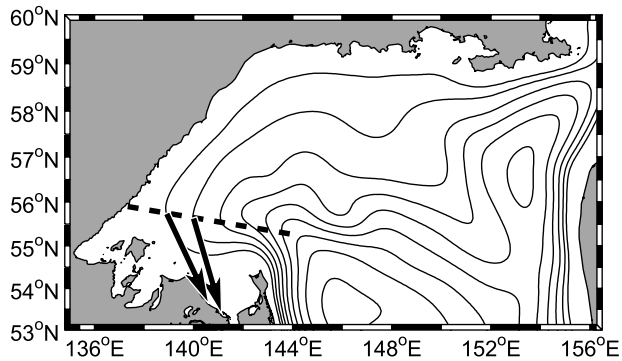

Figure 6. Planetary potential vorticity, f/h. The contour interval varies to produce evenly spaced contours. Arrows show the mean velocity observed at the moorings. Line of assumed constant velocity is also shown (dashed line).

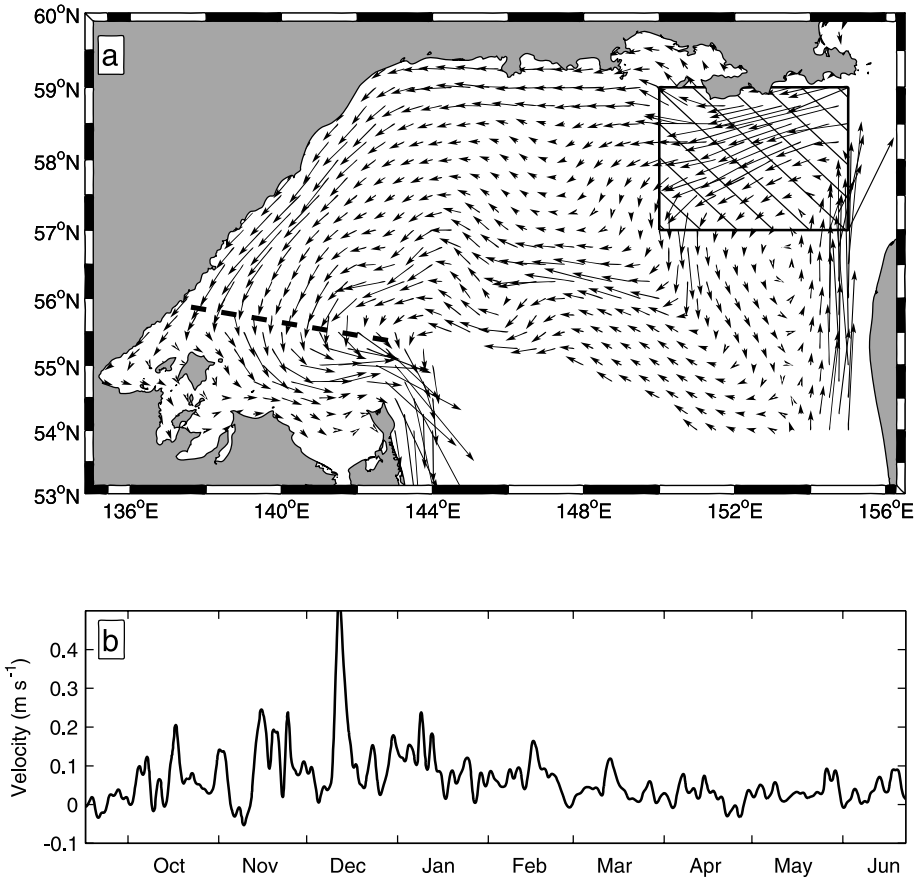

Figure 7. (a) Flow field used in the advective approach and (b) temporal variation of the flow amplitude, based on moored observations. Line of assumed constant velocity (dashed line) and "repopulation" region (hatching) are also shown in Figure 7a.

ment of the density anomaly inside the polynya leads to the formation of a rim current at the edge of the forcing region. This current later becomes baroclinically unstable and gives rise to a series of eddies, which effectively disperse the density anomaly. These processes result in an abrupt termination of density increase despite continuous forcing [*Gawarkiewicz and Chapman*, 1995], much like the termination observed at the inshore mooring [*Shcherbina et al.*, 2004]. Gross overestimation of maximum salinity at the site of inshore mooring by the advective method might be due to the exclusion of eddy transport balancing the salt influx in late February to late March. The missing DSW eddy transport during that period can be estimated as the difference between the production and along-isobath advective export rates, giving a mean value of 0.8 Sv from 23 February to 13 March. Consequently, the eddy transport may account for an additional 0.04 Sv of mean annual DSW export.

[36] On the other hand, the gradual salinity decrease at the inshore mooring in spring appears to be adequately described by the along-isobath advection model. This allows us to conclude that the final salinity of DSW at the end of brine rejection season decreases toward the northeast. The advection of this gradient past the mooring is responsible for the salinity decrease observed in spring and also continuing in the autumn, as apparent from the beginning of the record. This conclusion contradicts one of the assumptions of CM-94, which postulates a uniform salinity increase of the whole water mass.

4. Conclusion

[37] The mean annual production rate estimated from the heat loss in the northwestern polynya alone is 0.27 Sv. Comparison of the rates of salinity increase observed directly and inferred from the heat flux analysis suggests that the brine rejection rate based on heat flux data is underestimated by a factor of 0.74. Consequently, the estimate of mean annual production rate should be increased to 0.36 Sv. These estimates are consistent with the previous indirect estimates [*Martin et al.*, 1998; *Gladyshev et al.*, 2000, 2003], although direct comparison is difficult due to interannual variability. The winter of 1999–2000 was milder than usual [*Shcherbina et al.*, 2004], which may have led to a lower DSW production.

[38] Using the directly measured velocities, the export rate of Okhotsk Sea dense shelf water in 1999–2000 was found to vary between negligible in autumn, 0.75 ± 0.27 Sv in winter, and 0.34 ± 0.12 Sv in spring. Assuming the spring rates of export continued through the summer, the mean annual export rate of DSW is estimated to be 0.30 Sv. Additionally, cross-shelf eddy transport of DSW in late

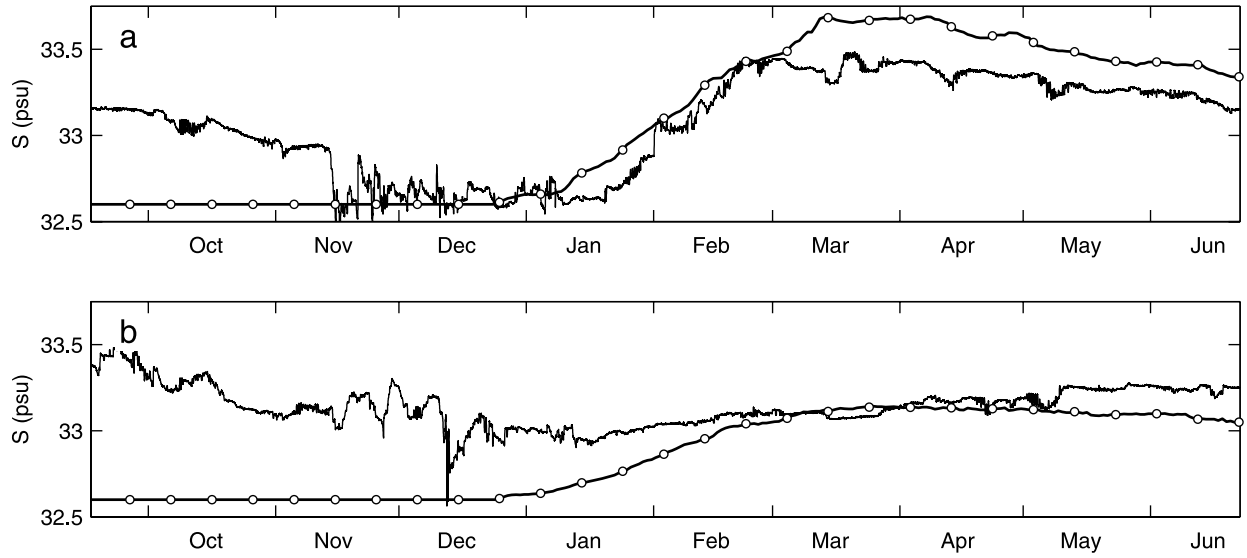

Figure 8. Advective estimate of DSW salinity evolution (line marked with dots every 10 days) and observed (solid line) salinity at the sites of the (a) inshore and (b) offshore moorings.

February to late March is estimated to contribute 0.04 Sv to the mean annual DSW export.

[39] The estimated annual DSW formation is quite small. However, its role in the thermahaline overturn of the North Pacific is significant. Theoretical [*Price and Baringer*, 1994] and observational studies in the North Atlantic [*Dickson and Brown*, 1994] and Arctic Ocean [*Fahrbach et al.*, 2001] alike show that entrainment and mixing lead to a roughly twofold increase of the volume transport of newly formed dense waters by the time they reach their equilibrium depth. Similarly, the transport of DSW in the Okhotsk Sea intensifies as the water travels southward along the Sakhalin coast. As a result, OSMW production is a factor of 3 to 4 greater than that of DSW [*Alfultis and Martin*, 1987; *Gladyshev et al.*, 2000, 2003]. Our observed DSW production rate is thus consistent (accounting for interannual variability) with the mean overturn of about 2 Sv between surface and intermediate layers [*Macdonald*, 1998; *Talley*, 2003] that sustains the NPIW.

Appendix A: Calculation of Heat Flux

[40] The net heat flux F_{net} consists of turbulent sensible (F_S) and latent or evaporative (F_E) heat fluxes, as well as net shortwave (F_R) and longwave (F_L) radiation,

$$F_{\text{net}} = F_S + F_E + F_R + F_L. \tag{A1}$$

Sensible and latent heat fluxes are calculated using the bulk formulae

$$F_S = \rho_a c_p C_S U (T_a - T_s) \tag{A2}$$

$$F_E = 0.622 \rho_a L_v C_E U (e - e_s), \tag{A3}$$

where ρ_a = 1.3 kg m^{-3} is the air density, c_p = 1004 J kg^{-1} K^{-1} is the specific heat at constant pressure, L_v is the latent heat of vaporization (2.52×10^6 J kg^{-1} for water and 2.86×10^6 J kg^{-1} for ice), C_S and C_E are stability dependent bulk transfer coefficients [*Kondo*, 1975], U is the wind speed, T_a and T_s are air and surface temperatures, e is the water vapor pressure, and e_s is the saturated water vapor pressure at the surface temperature.

[41] ECMWF reanalysis data for 2-m surface air temperature and 10-m surface wind speed are given as T_a and U, respectively. Following *Ohshima et al.* [2003], who found a 25% difference between the European Centre for Medium-Range Weather Forecasts (ECMWF) wind data and observations, U is corrected by a factor of 1.25. The water vapor pressure e is calculated as the saturated water vapor pressure at the ECMWF 2-m surface dew point temperature. The surface temperature T_s is taken to be -1.8°C (freezing point) for water and is estimated iteratively for ice (see below).

[42] Radiative fluxes are estimated using the parameterizations found to be optimal for arctic conditions [*Key et al.*, 1996]. For the shortwave radiation, the empirical formula by *Jacobs* [1978] gives

$$F_R = (1 - \alpha)(1 - 0.33C) F_{R0}, \tag{A4}$$

where α is the surface albedo, C = 0.7 is the mean fractional cloud cover, and F_{R0} is the mean daily incoming solar radiation, estimated using the *Zillman* [1972] empirical formula. Albedos of 0.06, 0.27, 0.36, and 0.64 were assumed for open water, new, young, and first-year ice, respectively [*Ohshima et al.*, 2003]. Longwave radiation is estimated as

$$F_L = \varepsilon_s \sigma T_s^4 - \varepsilon_a \sigma T_a^4, \tag{A5}$$

where ε_s is the surface emissivity (0.97 for water, 0.99 for ice), $\sigma = 5.67 \times 10^{-8}$ W m^{-2} K^{-4} is the Stefan-Boltzman constant, and ε_{a} is the effective atmosphere emissivity, given by combining the empirical formulae of *Efimova* [1961] and *Jacobs* [1978],

$$\varepsilon_a = (0.746 + 0.0066e)(1 + 0.26C), \tag{A6}$$

where e is the water vapor pressure.

[43] For the ice-covered areas the net surface flux should be equal to the conductive heat flux through the ice,

$$F_c = k(T_w - T_s)/d, \quad \text{(A7)}$$

where $k = 2.1$ W m^{-1} K^{-1} is the ice heat conductivity, T_w is the water temperature, and d is the ice thickness.

[44] The ice thickness is the major uncertainty in estimation of the ice heat fluxes, as it has to be estimated using the SSM/I data without much observational background. On the basis of historical data, *Ohshima et al.* [2003] used the values of 5, 20, and 80 cm for new, young, and first-year ice, respectively; 16-cm snow cover was also assumed for the first-year ice, bringing its "effective" thickness to 1.85 m. For the present study, we chose d to be an empirical piecewise linear function of the ice type parameter, which was derived from the 19 GHz polarization ratio [*Kimura and Wakatsuchi*, 1999]. This choice led to a more natural continuous ice thickness variation: 5–10 cm for new, 10–30 cm for young, and 30–80 cm for first-year ice.

[45] The ice surface temperature that satisfies the balance $F = F_c$ was computed iteratively, starting with $T_s = 0.6T_a$. On each iteration step the surface heat fluxes were estimated using equation (A1), and then equation (A7) was used to obtain the updated ice surface temperature that satisfies the balance. Just a few iterations were enough to achieve a stable value of T_s.

[46] **Acknowledgments.** This work was supported through the National Science Foundation grant OCE-9811958 and by Hokkaido University (ship support). Technical support was provided by the Oceanographic Data Facility and the Instrument Development Group at Scripps Institution of Oceanography (SIO), and by the captain and crew of the R/V *Professor Khromov*. We thank S. Gladyshev, K. Ohshima, and S. Martin for helpful discussion of heat flux calculations in the ice-covered Okhotsk Sea.

References

Alfultis, M. A., and S. Martin (1987), Satellite passive microwave studies of the Sea of Okhotsk ice cover and its relation to oceanic processes, *J. Geophys. Res.*, *92*, 13,013–13,028.

Cavalieri, D. (1994), A microwave technique for mapping thin sea ice, *J. Geophys. Res.*, *99*, 12,561–12,572.

Cavalieri, D. J., and S. Martin (1994), The contribution of Alaskan, Siberian, and Canadian coastal polynyas to the cold halocline layer of the Arctic Ocean, *J. Geophys. Res.*, *99*, 18,343–18,362.

Dickson, R. R., and J. Brown (1994), The production of North Atlantic Deep Water: Sources, rates, and pathways, *J. Geophys. Res.*, *99*, 12,319–12,341.

Efimova, N. A. (1961), On methods of calculating monthly values of net longwave radiation, *Meteorol. Gidrol.*, *10*, 28–33.

Fahrbach, E., S. Harms, G. Rohardt, M. Schröder, and R. Woodgate (2001), Flow of bottom water in the northwestern Weddell Sea, *J. Geophys. Res.*, *106*, 2761–2778.

Gawarkiewicz, G., and D. Chapman (1995), A numerical study of dense water formation and transport on a shallow, sloping continental shelf, *J. Geophys. Res.*, *100*, 4489–4507.

Gladyshev, S., S. Martin, S. Riser, and A. Figurkin (2000), Dense water production on the northern Okhotsk shelves: Comparison of ship-based spring-summer observations for 1996 and 1997 with satellite observations, *J. Geophys. Res.*, *105*, 26,281–26,299.

Gladyshev, S., L. Talley, G. Kantakov, G. Khen, and M. Wakatsuchi (2003), Distribution, formation, and seasonal variability of Okhotsk Sea Mode Water, *J. Geophys. Res.*, *108*(C6), 3186, doi:10.1029/2001JC000877.

Haarpaintner, J., J. C. Gascard, and P. M. Haugan (2001), Ice production and brine formation in Storfjorden, Svalbard, *J. Geophys. Res.*, *106*, 14,001–14,013.

Itoh, M., K. I. Ohshima, and M. Wakatsuchi (2003), Distribution and formation of Okhotsk Sea Intermediate Water: An analysis of isopycnal climatological data, *J. Geophys. Res.*, *108*(C8), 3258, doi:10.1029/2002JC001590.

Jacobs, J. D. (1978), Radiation climate of Broughton Island, in *Energy Budget Studies in Relation to Fast-Ice Breakup Processes in Davis Strait*, edited by R. G. Barry and J. D. Jacobs, *Occas. Pap. 26*, pp. 105–120, Inst. of Arctic and Alp. Res., Univ. of Colo., Boulder.

Key, J. R., R. A. Silcox, and R. S. Stone (1996), Evaluation of surface radiative flux parameterizations for use in sea ice models, *J. Geophys. Res.*, *101*, 3839–3849.

Kimura, N., and M. Wakatsuchi (1999), Processes controlling the advance and retreat of sea ice in the Sea of Okhotsk, *J. Geophys. Res.*, *104*, 11,137–11,150.

Kitani, K. (1973), An oceanographic study of the Okhotsk Sea—Particularly in regard to cold waters, *Bull. Far Seas Fish. Res. Lab.*, *9*, 45–76.

Kondo, J. (1975), Air-sea bulk transfer coefficient in diabatic conditions, *Boundary Layer Meteorol.*, *9*, 91–112.

Macdonald, A. M. (1998), The global ocean circulation: A hydrographic estimate and regional analysis, *Prog. Oceanogr.*, *41*, 281–382.

Martin, S., R. Drucker, and K. Yamashita (1998), The production of ice and dense shelf water in the Okhotsk Sea polynyas, *J. Geophys. Res.*, *103*, 27,771–27,782.

Maslanik, J., and J. Stroeve (2003), *DMSP SSM/I Daily Polar Gridded Brightness Temperatures* [CD-ROM], Natl. Snow and Ice Data Cent., Boulder, Colo.

Ohshima, K. I., T. Watanabe, and S. Nihashi (2003), Surface heat budget of the Sea of Okhotsk during 1987–2001 and the role of sea ice on it, *J. Meteorol. Soc. Jpn.*, *81*(4), 653–677.

Pedlosky, J. (1987), *Geophysical Fluid Dynamics*, 2nd ed., Springer-Verlag, New York.

Price, J. F., and M. Baringer (1994), Outflows and deep water production by marginal seas, *Prog. Oceanogr.*, *33*, 161–200.

Shcherbina, A. Y., L. D. Talley, and D. L. Rudnick (2003), Direct observations of North Pacific ventilation: Brine rejection in the Okhotsk Sea, *Science*, *302*(5652), 1952–1955.

Shcherbina, A. Y., L. D. Talley, and D. L. Rudnick (2004), Dense water formation on the northwestern shelf of the Okhotsk Sea: 1. Direct observations of brine rejection, *J. Geophys. Res.*, *109*, C09S08, doi:10.1029/2003JC002196, in press.

Talley, L. D. (1991), An Okhotsk water anomaly: Implications for ventilation in the North Pacific, *Deep Sea Res.*, *38*, Suppl. 1, S171–S190.

Talley, L. (1993), Distribution and formation of the North Pacific Intermediate Water, *J. Phys. Oceanogr.*, *23*, 517–537.

Talley, L. D. (2003), Shallow, intermediate, and deep overturning components of the global heat budget, *J. Phys. Oceanogr.*, *33*, 530–560.

Wong, C. S., R. J. Matear, H. J. Freeland, F. A. Whitney, and A. S. Bychkov (1998), WOCE line P1W in the Sea of Okhotsk: 2. CFCs and the formation rate of intermediate water, *J. Geophys. Res.*, *103*, 15,625–15,642.

Yasuda, I. (1997), The origin of the North Pacific Intermediate Water, *J. Geophys. Res.*, *102*, 893–909.

Zillman, J. W. (1972), A study of some aspects of the radiation and heat budgets of the Southern Hemisphere oceans, *Meteorol. Stud. Rep. 26*, Bur. of Meteorol., Dep. of the Inter., Canberra, Australia.

D. L. Rudnick, A. Y. Shcherbina, and L. D. Talley, Scripps Institution of Oceanography, University of California, San Diego, 9500 Gilman Drive, Mail Code 0230, La Jolla, CA 92093-0230, USA. (ashcherbina@ucsd.edu)